AGU PUBLICATIONS

Paleoceanography

RESEARCH ARTICLE
10.1002/2014PA002653

Middle Miocene climate instability associated with high-amplitude CO_2 variability

Rosanna Greenop[1], Gavin L. Foster[1], Paul A. Wilson[1], and Caroline H. Lear[2]

[1]National Oceanography Centre, Southampton, University of Southampton, Southampton, UK, [2]School of Earth and Ocean Sciences, Cardiff University, Cardiff, UK

Key Points:
- The middle Miocene is characterized by CO_2 variability between 300 and 500 ppm
- The high-amplitude CO_2 variability is matched by the changes in the paleorecords
- Two regimes of ice volume-CO_2 variability identified in middle Miocene

Supporting Information:
- Readme
- Table S1

Correspondence to:
R. Greenop,
r.greenop@noc.soton.ac.uk

Citation:
Greenop, R., G. L. Foster, P. A. Wilson, and C. H. Lear (2014), Middle Miocene climate instability associated with high-amplitude CO_2 variability, *Paleoceanography*, *29*, 845–853, doi:10.1002/2014PA002653.

Received 4 APR 2014
Accepted 6 AUG 2014
Accepted article online 11 AUG 2014
Published online 4 SEP 2014

The copyright line for this article was changed on 30 SEP 2014 after original online publication.

Abstract The amplitude of climatic change, as recorded in the benthic oxygen isotope record, has varied throughout geological time. During the late Pleistocene, changes in the atmospheric concentration of carbon dioxide (CO_2) are an important control on this amplitude of variability. The contribution of CO_2 to climate variability during the pre-Quaternary however is unknown. Here we present a new boron isotope-based CO_2 record for the transition into the middle Miocene Climatic Optimum (MCO) between 15.5 and 17 Myr that shows pronounced variability between 300 ppm and 500 ppm on a roughly 100 kyr time scale during the MCO. The CO_2 changes reconstructed for the Miocene are ~2 times larger in absolute terms (300 to 500 ppm compared to 180 to 280 ppm) than those associated with the late Pleistocene and ~15% larger in terms of climate forcing. In contrast, however, variability in the contemporaneous benthic oxygen isotope record (at ~1‰) is approximately two thirds the amplitude of that seen during the late Pleistocene. These observations indicate a lower overall sensitivity to CO_2 forcing for Miocene (Antarctic only) ice sheets than their late Pleistocene (Antarctic plus lower latitude northern hemisphere) counterparts. When our Miocene CO_2 record is compared to the estimated changes in contemporaneous $\delta^{18}O_{sw}$ (ice volume), they point to the existence of two reservoirs of ice on Antarctica. One of these reservoirs appears stable, while a second reservoir shows a level of dynamism that contradicts the results of coupled climate-ice sheet model experiments given the CO_2 concentrations that we reconstruct.

1. Introduction

Variations in the orbit of the Earth around the Sun have paced the Earth's climate cycles throughout geological time; however, the amplitude of the change in radiative forcing caused by orbital variations is too small to directly drive the observed magnitude of the climate change [*Hays et al.*, 1976]. Instead, feedbacks in the Earth system must exist to amplify the changes in orbital forcing [*Imbrie et al.*, 1993; *Shackleton*, 2000]. In the case of the glacial-interglacial cycles of the late Pleistocene when variability in the benthic oxygen isotope record was high (1.5‰), the changes in radiative forcing brought about by CO_2 change were relatively large (up to $-2.4\ W/m^2$), identifying CO_2 as an important contributor to climate variability over the past 800,000 years [*Köhler et al.*, 2010; *Lisiecki and Raymo*, 2005; *Lüthi et al.*, 2008]. However, it is not known whether the role played by CO_2 in climate variability over the past 800,000 years is unique to the late Pleistocene. In fact, the lack of suitable records has prevented the analysis of the role of CO_2 in controlling climate variability in the pre-Quaternary.

One pre-Quaternary time interval that exhibits significant fluctuations in climate as recorded by change in the benthic $\delta^{18}O$ record is the middle Miocene Climatic Optimum (MCO) between 14.7 and 17 Ma [*Holbourn et al.*, 2007; *Holbourn et al.*, 2014]. The MCO is a generally warm time interval punctuating the long-term Cenozoic cooling trend (Figure 1) [*Zachos et al.*, 2008]. Global mean temperatures are estimated to have been around 2 to 4°C warmer than the preindustrial temperatures with the largest temperature differences to modern in the high latitudes [*Warny et al.*, 2009; *You et al.*, 2009]. Palynological data from ANtarctic geological DRILLing (ANDRILL) AND-2A, near the modern ice margin of the East Antarctic ice sheet in the Ross Sea, suggest that circum-Antarctic annual sea surface temperatures ranged from 0 to 11.5°C (compared to ~ −1 to 3°C today [*Schlitzer*, 2000]) with January mean land temperatures ~11°C warmer than today during the peak MCO warmth [*Warny et al.*, 2009]. A further striking feature of the MCO is the smaller and more dynamic ice sheet on Antarctica that is thought to have accompanied these warmer high-latitude temperatures [*Billups and Schrag*, 2002; *Fielding et al.*, 2011; *Holbourn et al.*, 2007; *Holbourn et al.*, 2014; *Passchier et al.*, 2011; *Shevenell et al.*, 2004; *Warny et al.*, 2009]. Sedimentary facies analysis conducted on

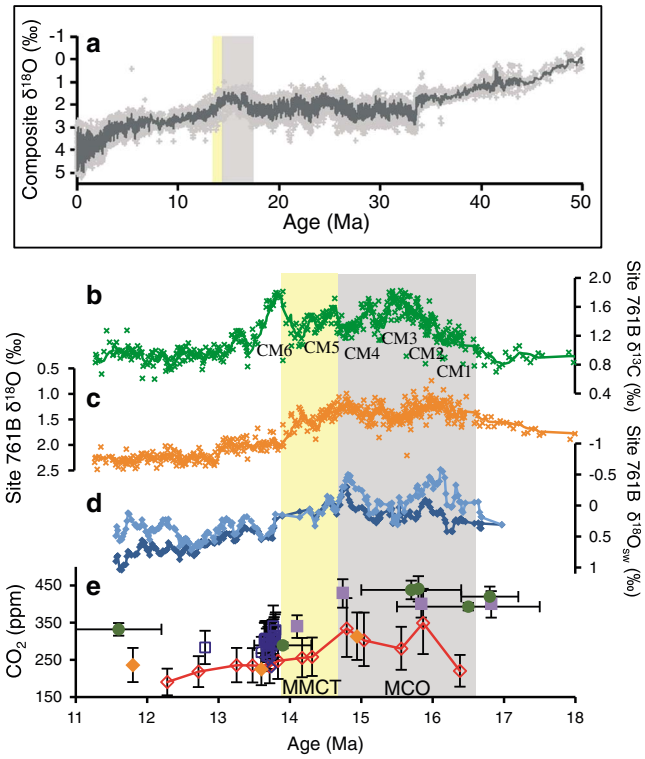

Figure 1. Long-term climate and pCO_2 records from the middle Miocene. (a) Composite benthic $\delta^{18}O$ with 5 point moving average [*Zachos et al.*, 2008]. Grey and yellow bars indicate the middle Miocene Climatic Optimum (MCO) and mid-Miocene Climatic Transition (MMCT), respectively. (b and c) Benthic $\delta^{13}C$ and $\delta^{18}O$ records from Site 761B with 5 point moving average [*Holbourn et al.*, 2004; *Lear et al.*, 2010]. CM are the carbon maxima events as identified at 761B by *Holbourn et al.* [2004]. (d) Seawater $\delta^{18}O$ (‰ versus Pee Dee belemnite (PDB)) [*Lear et al.*, 2010]. The light blue data points are calculated assuming a carbonate ion effect on the Mg/Ca ratios, while the dark blue points are calculated assuming no carbonate ion effect on measured Mg/Ca. (e) CO_2 from boron isotopes ($\delta^{11}B$); (red open diamonds (Site 761B) [*Foster et al.*, 2012], orange solid diamonds (Site 926) [*Foster et al.*, 2012], and open dark blue diamonds [*Badger et al.*, 2013]); leaf stomata (dark green circles [*Kürschner et al.*, 2008]); and alkenones (open dark blue squares [*Badger et al.*, 2013] and purple squares [*Zhang et al.*, 2013]).

AND-2A shows evidence for large-amplitude cyclicity in facies associations in middle Miocene strata. These cycles are interpreted to indicate changes from open water to ice-proximal deposition during the early middle Miocene with two discrete intervals of ice sheet and sea ice minima at ~15.7 Ma and ~16.4 Ma [*Acton et al.*, 2008–2009; *Fielding et al.*, 2011; *Passchier et al.*, 2011; *Warny et al.*, 2009]. A strong orbital control on climate variability in the middle Miocene is clearly seen in high-resolution benthic oxygen isotope records, which are characterized by high-amplitude (~1‰) variability during the MCO with a periodicity matching that of the short-term (~100 kyr) eccentricity cycle [*Holbourn et al.*, 2007; *Holbourn et al.*, 2014]. A similar orbital pacing (94–99 kyr) is seen in particle size data from AND-2A and interpreted to reflect the hydrodynamic effects of wave stirring in response to ice sheet growth and decay (intensity of wave stirring is controlled by the effect of the ice sheet on various high-latitude climate system parameters such as iceberg density) [*Passchier et al.*, 2013]. Yet as with the well-documented climate cycles of the late Pleistocene, climate variations with an eccentricity pacing are difficult to explain. One long-standing problem is that the amplitude of change in radiative forcing brought about by eccentricity change is too small to drive climate variability directly [*Imbrie et al.*, 1993; *Shackleton*, 2000]. Another problem concerns the lack of evidence for major ice expansion during the minimum or "node" in the obliquity amplitude modulation centered around 16.2 Ma, when we might predict ice expansion in response to dampened seasonal extremes, particularly the suppression of ablation-inducing warm summers [*Holbourn et al.*, 2007]. In fact, this predicted expansion of glacial conditions is not seen until 2.4 Myr later, at the mid-Miocene Climatic Transition (MMCT), during a node in obliquity no more extreme than the one at 16.2 Ma. These observations indicate that orbital forcing alone cannot fully explain the observed mid-Miocene climate history and that some additional factors must have exerted a fundamental control on the climate system at this time. A number of recent studies have suggested that variations in atmospheric CO_2 drive long-term Miocene climate change [*Foster et al.*, 2012; *Kürschner et al.*, 2008]. Published estimates of atmospheric CO_2 fall in the range of 200 to 450 ppm during the MCO (Figure 1e) [*Foster et al.*, 2012; *Kürschner et al.*, 2008]. Yet the resolution of these records is too crude, and the discrepancies among different proxies are currently too large to provide an insight into the possible role of CO_2 in amplifying shorter-term climate variability during the MCO. Here we present a new higher-resolution boron isotope-based $\delta^{11}B$-CO_2 record and use this to assess the relationship between climate and CO_2 variability in the middle Miocene.

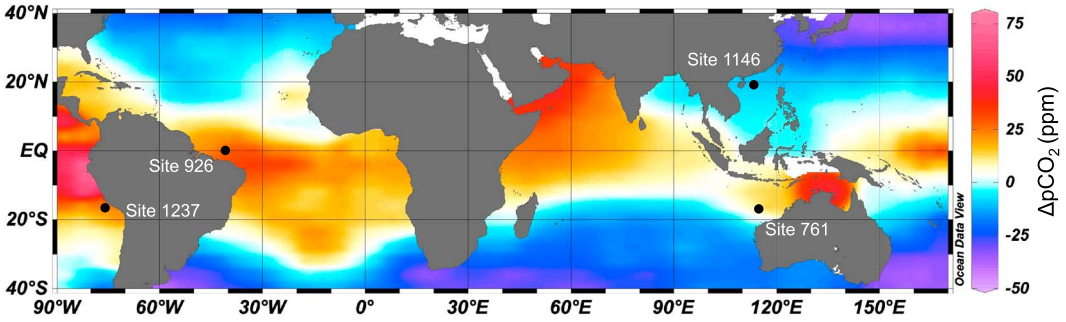

Figure 2. Map of study sites and mean annual air-sea disequilibria with respect to pCO_2. The black dots indicate the location of the sites referred to in this study. ODP Site 761 (16°44.23′S, 115°32.10′E) is from a water depth of 2179 m. The modern extent of disequilibria at Site 761B is <25 ppm. ODP Site 926 (3°43.148′N, 42°54.507′W), ODP Site 1237 (16°0.421′S, 76°22.685′W), and ODP Site 1146 (19°27.40′N, 116°16.37′E) are also plotted for reference. Data are from *Takahashi et al*. [2009].

2. Materials and Methods

To better understand the role of greenhouse gas forcing in climate variability across the MCO, a CO_2 record of higher temporal resolution is needed. We exploit sediments of Miocene age from Ocean Drilling Program (ODP) Hole 761B (16°44.23′S, 115°32.10′E) in the Indian Ocean (Figure 2). The foraminifera sampled from ODP Hole 761B were taken from 47 to 52 m below seafloor (meters composite depth). The $\delta^{18}O$ and $\delta^{13}C$ stratigraphies for Hole 761B are not sufficiently structured to allow the development of a reliable orbitally tuned age model, but both of these records capture the characteristic structure that typically defines the long-term climate evolution of the middle Miocene seen at other sites (Figures 1 and 3) [*Holbourn et al*., 2004; *Lear et al*., 2010]. The oxygen isotope stratigraphy was used to capture the full range of climate variability, and measurements were made with ~40 kyr spacing. Surface waters at this site today are close to equilibrium with the atmosphere with respect to CO_2 (Figure 2) [*Takahashi et al*., 2009]. Boron isotope measurements (described in delta notation as $\delta^{11}B$—per mil variation from the boric acid Standard Reference Material 951 [*Catanzaro et al*., 1970]) were made on the $CaCO_3$ shells of the mixed layer dwelling foraminifera *Globigerinoides trilobus* (300–355 μm). Boron was first separated from the Ca matrix prior to analysis using the boron specific resin Amberlite IRA 743 following *Foster* [2008]. The boron isotopic composition was then determined using a sample-standard bracketing routine on a Thermo Fisher Scientific Neptune multicollector inductively coupled plasma mass spectrometer at the University of Southampton (closely following *Henehan et al*. [2013]). The

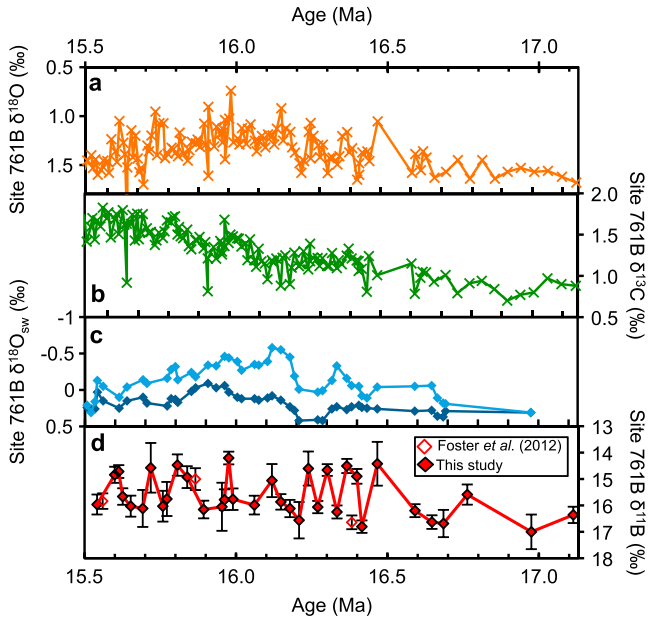

Figure 3. MCO climate proxies with the new boron isotope data ($\delta^{11}B$). (a–c) Benthic $\delta^{18}O$, $\delta^{13}C$, and seawater $\delta^{18}O$ records from Site 761B between 15.5 and 17.13 Myr. For the $\delta^{18}O_{sw}$, the light blue data points are calculated assuming a carbonate ion effect on the Mg/Ca ratios, while the dark blue points are calculated assuming no carbonate ion effect on measured Mg/Ca [*Holbourn et al*., 2004; *Lear et al*., 2010]. (d) The $\delta^{11}B$ from Site 761B (solid diamonds from this study and open diamonds from *Foster et al*. [2012]). The $\delta^{11}B$ are measured against the National Institute of Standards and Technology SRM boric acid standard 951. Note the inverted axis. The error bars show 2 standard deviation external reproducibility.

$\delta^{11}B$ in planktic foraminiferal calcite, such as *G. trilobus* [*Sanyal et al*., 2001], correlates positively with pH and negatively with $[CO_2]_{aq}$ [*Foster*, 2008; *Sanyal et al*., 2000]. In the absence of changes in the local hydrography, variations of atmospheric CO_2 are the dominant influence on $[CO_2]_{aq}$. Previous work at ODP Site 761 during the Miocene has shown that $\delta^{11}B$-derived CO_2 is reproducible at ODP Site 926 and in broad agreement with other methods of reconstructing CO_2 (Figure 1), suggesting that variations in atmospheric CO_2 are the dominant control on $\delta^{11}B$ variability at our study site [*Foster et al*., 2012].

To put the relative changes in CO_2 during the middle Miocene captured by our $\delta^{11}B$ data set in context, it is instructive to make absolute reconstructions of CO_2. To calculate CO_2 from $\delta^{11}B$, several other parameters are needed. First, sea surface temperatures (SSTs) and sea surface salinities (SSSs) are required to calculate the pK_B of boric acid [*Dickson*, 1990]. Here SSTs are calculated from tandem Mg/Ca analyses on *G. trilobus* with adjustments for Mg/Ca_{sw} from *Horita et al*. [2002] (with a conservative ±3°C) using the calibration of *Anand et al*. [2003] while SSS is held constant at 35 ± 3‰ for the entire record. These variables only have a minor affect on the calculated pH and pCO_2 (~30 ppm for a ±3°C; ± ~10 ppm for a ±3‰). Second, $\delta^{11}B_{sw}$ during the middle Miocene is an important source of uncertainty and can have a significant effect on the calculation of absolute CO_2. The residence time of boron in the oceans is long (~10 to 20 Myr), ensuring that major changes in $\delta^{11}B_{sw}$ are unlikely during our 1.5 Myr long study [*Lemarchand et al*., 2002]. It is probable however that $\delta^{11}B_{sw}$ in the Miocene was different to the present value of 39.61‰, and here we use a $\delta^{11}B_{sw}$ value of 37.82 ± 0.7‰, determined for the middle Miocene using the offsets in $\delta^{11}B$ between benthic and planktic foraminifera [*Foster et al*., 2010, 2012]. Third, to define atmospheric CO_2, a second carbonate system parameter is needed. Here we use a total alkalinity value of 1292 ± 300 μmol/kg determined by *Foster et al*. [2012] for the middle Miocene and constrained by reconstructions of the calcium carbonate compensation depth (CCD) [*Sime et al*., 2007] and deepwater pH reconstructions [*Foster et al*., 2012]. A change in the depth of the CCD by ±500 m results in variations of ±100 μmol/kg in the estimation of deepwater alkalinity. The ±300 μmol/kg uncertainty on the alkalinity estimate used in this study should therefore account for any rapid changes in CCD, across this interval, that may not be fully resolved in the lower resolution CCD records [*Sime et al*., 2007]. A full propagation of uncertainty on our CO_2 estimate is carried out using a Monte Carlo simulation ($n = 10{,}000$) using the uncertainty limits highlighted above. The Monte Carlo simulation allows us to fully account for the combined effect of the required parameters on the calculated CO_2, and our overall uncertainty in our CO_2 estimates using this technique is calculated to be ±66–353 ppm (95% confidence interval). These estimates include uncertainties in the $\delta^{11}B$ measurement, SST, SSS, total alkalinity, and $\delta^{11}B$ seawater as outlined above. The uncertainties in the other parameters needed to calculate CO_2, aside from the *G. trilobus* $\delta^{11}B$, are larger (by a factor of 1.5 to 2) in this study than those reported by *Foster et al*. [2012] to reflect greater potential variability in these parameters over the shorter time scales investigated here and any secular evolution between the time interval, when $\delta^{11}B_{sw}$ and total alkalinty were determined by *Foster et al*. [2012] and this study interval (12.72 Ma versus 15.5–17 Ma).

3. Results and Discussion

In Figure 3, alongside published stable isotope records, we present a new boron isotope data set spanning 15.5 to 17 Myr from Site 761B. This new boron isotope record shows high $\delta^{11}B$ values (16 to 17.5‰; hence lowest CO_2) during the interval 17 to 16.5 Ma leading up to the MCO. During the MCO (16.5 to 15.5 Ma), the $\delta^{11}B$ record shows pronounced variability with the presence of distinctly lower values (16.5 to 14.5‰; hence higher CO_2) (Figure 3). The 1.5 to 2‰ changes in $\delta^{11}B$ suggest that CO_2 variability is closely linked to the observed pronounced variability in high-latitude climate during the MCO. Our data therefore confirm inferences made from the $\%CaCO_3$ content of deep ocean sediments from the equatorial Pacific [*Holbourn et al*., 2014] that large variations in the carbon cycle accompanied climate variability during the MCO. The minima in $\delta^{11}B$ in our record appear to occur with a rough 100 kyr spacing, raising the question of whether they might be paced by the short eccentricity cycle. However, our $\delta^{11}B$ data are not of sufficiently high temporal resolution to address this question quantitatively. Furthermore, while comparison of records at Site 761B shows some similarities of the appropriate sign ($\delta^{11}B$ maxima with $\delta^{18}O$ minima), the Site 761B $\delta^{18}O$ record does not demonstrate clear 100 kyr cyclicity (Figure 3). This lack of clear orbital cyclicity in the oxygen also prohibits detailed correlation of our $\delta^{11}B$ record to other, better resolved oxygen isotope stratigraphies. Therefore, while our $\delta^{11}B$ record documents the existence of short-term CO_2 variability in the pre-Quaternary, work elsewhere is

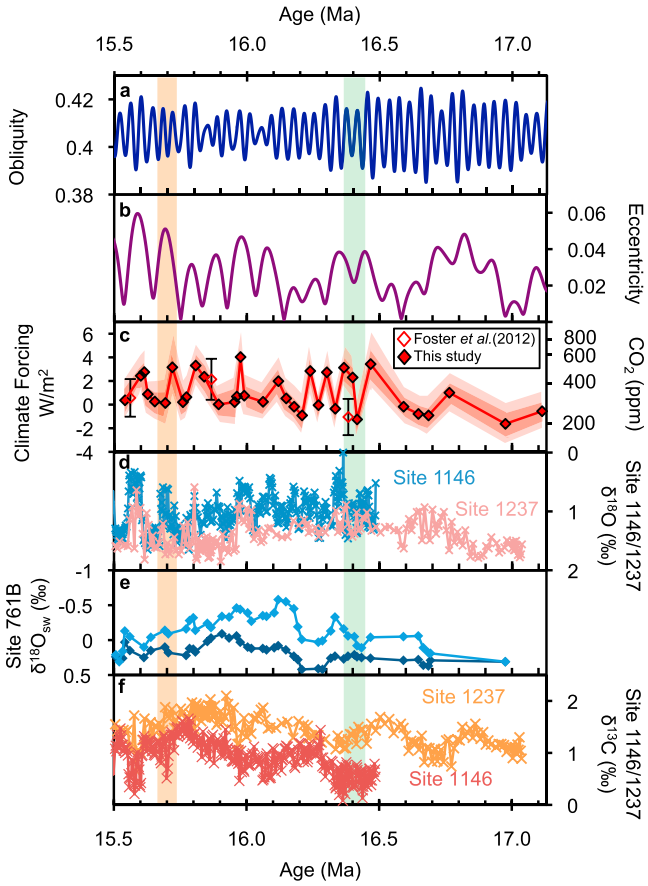

Figure 4. High-amplitude changes in MCO climate records and CO_2. (a and b) Obliquity and eccentricity cycles [*Laskar et al.*, 2004]. (c) CO_2 reconstruction for ODP Site 761B plotted as CO_2 and climate forcing ($\Delta F = 5.35*\ln(C/C_0)$ W/m^2, where C is the CO_2 concentration in parts per million and C_0 is the reference preindustrial concentration (280 ppm) [*Myhre et al.*, 1998]) (closed diamonds (this study) and open diamonds from *Foster et al.* [2012]). CO_2 is calculated using a surface water total alkalinity (~1293 ± 300 μmol/kg) and a $\delta^{11}B_{sw} = 37.82 \pm 0.7$‰. The pale red band on the δ^{11}B-CO_2 record shows the climate forcing/CO_2 uncertainty at 95% confidence interval and the dark red band at 68% confidence interval for the data from this study. The error bars on *Foster et al.*'s [2012] data show climate forcing/CO_2 uncertainty at 95% confidence interval. (d) Benthic δ^{18}O record at ODP Site 1146 and ODP Site 1237 [*Holbourn et al.*, 2007]. (e) Seawater δ^{18}O (‰ versus PDB) [*Lear et al.*, 2010]. The light blue data points are calculated assuming a carbonate ion effect on the Mg/Ca ratios, while the dark blue points are calculated assuming no carbonate ion effect on measured Mg/Ca. (f) Benthic δ^{13}C record at ODP Site 1146 and ODP Site 1237 [*Holbourn et al.*, 2007]. The orange and green vertical bars highlight the major ice sheet retreat at ~15.7 Ma and ~16.4 Ma, respectively [*Acton et al.*, 2008–2009; *Fielding et al.*, 2011; *Passchier et al.*, 2011; *Warny et al.*, 2009].

required to gain a fuller understanding of the links between CO_2 and climate on orbital time scales during the middle Miocene.

Despite this inability to fully quantify the cyclicity within our new δ^{11}B record, our new data indicate that CO_2 oscillated from a baseline value of 250 to 350 ppm to a maximum of ~500 ppm, a value that is reached at several times during the MCO (±66–353 ppm, 95% confidence interval) (Figure 4). The CO_2 minima and maxima in our new record fall close to the range of MCO values previously reported using a number of different techniques [*Foster et al.*, 2012; *Kürschner et al.*, 2008; *Zhang et al.*, 2013]. The new record exhibits, however, considerably more structure than is seen in published data sets and goes some way to reconciling some of the differences among those existing CO_2 records. The maximum values for CO_2 that we calculate (~500 ppm) also fall within the range required in climate models to match the observed warmth during the MCO (e.g., 460–580 ppm [*You et al.*, 2009]).

CO_2 exerts a logarithmic forcing on global climate defined by the relationship: climate forcing = $5.35*\ln(C/C_0)$ W/m^2, where C is the CO_2 concentration in ppm and C_0 is the reference preindustrial concentration (278 ppm) [*Myhre et al.*, 1998]. The range in CO_2 (interglacial-glacial variability) that we reconstruct is ~2 times larger in absolute terms than that associated with the late Pleistocene climate change [*Lüthi et al.*, 2008], but the logarithmic relationship between CO_2 and climate forcing means that the resulting increase in the range of radiative forcing is more modest (only ~15% larger than the late Pleistocene). Nevertheless, the larger range in radiative forcing for the Miocene than for the late Pleistocene sharply contrasts with the observed variability in climate as measured in the benthic oxygen isotope record (glacial-interglacial variability in benthic δ^{18}O during the Miocene is only about two thirds of that seen during the late Pleistocene [*Holbourn et al.*, 2014; *Lisiecki and Raymo*, 2005]). This observation suggests that larger CO_2 changes are required to induce changes in temperature and ice volume during the Miocene than for the late Pleistocene. We interpret this result to reflect the impact of the absence during the MCO of large ice sheets in the northern hemisphere (where ice sheets accumulate at lower latitudes than in the southern hemisphere and where the thermal response to transient CO_2 increase is greater because of a larger land area in the sensitive

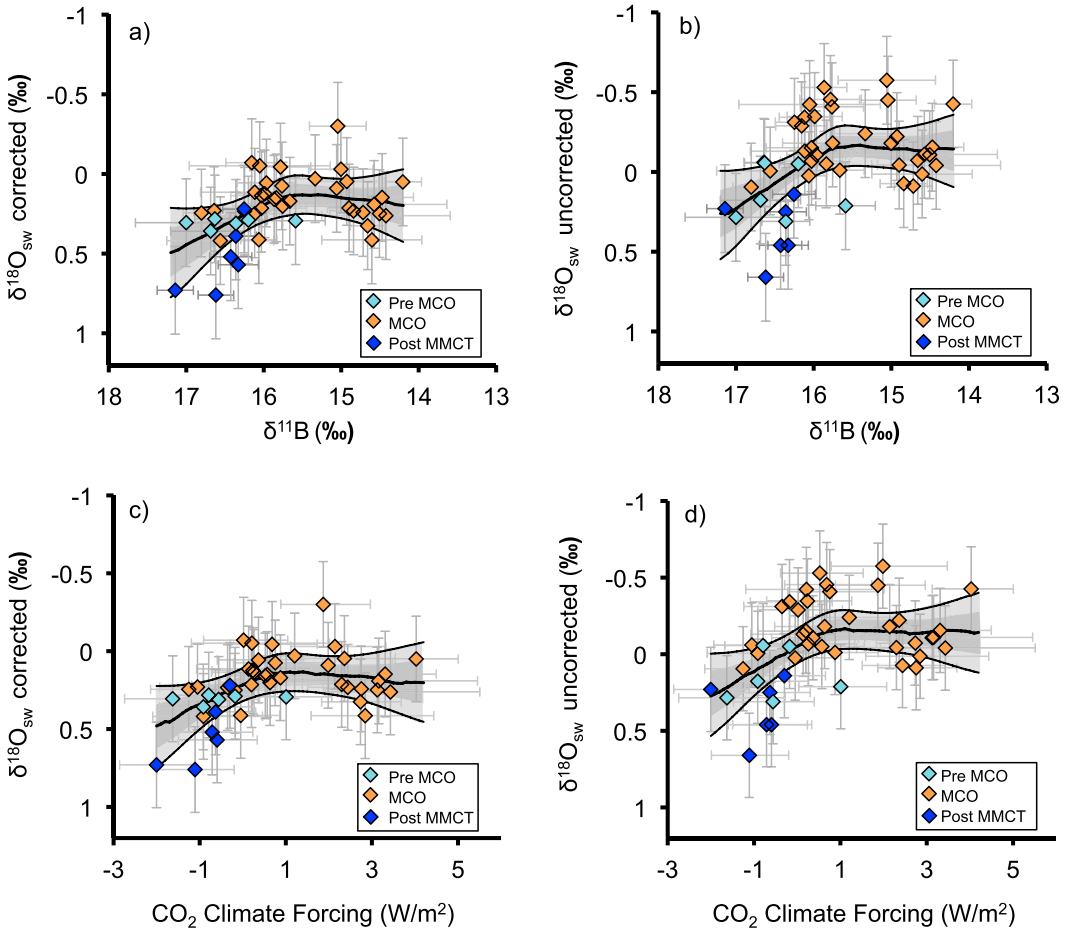

Figure 5. Crossplots of δ^{11}B/climate forcing and $\delta^{18}O_{sw}$. For $\delta^{18}O_{sw}$ calculations [see *Lear et al.*, 2010]. (a) The $\delta^{18}O_{sw}$ calculated assuming a carbonate saturation state effect on Mg/Ca plotted with *G. trilobus* δ^{11}B. (b) The $\delta^{18}O_{sw}$ calculated assuming no carbonate saturation state effect on Mg/Ca plotted with *G. trilobus* δ^{11}B. (c) The $\delta^{18}O_{sw}$ calculated assuming a carbonate saturation state effect on Mg/Ca plotted with climate forcing (as defined in text). (d) The $\delta^{18}O_{sw}$ calculated assuming no carbonate saturation state effect on Mg/Ca plotted with climate forcing. The δ^{11}B/climate forcing data from this study and *Foster et al.* [2012] and the error bars show either analytical uncertainty (for δ^{11}B) or reconstructed uncertainty (climate forcing, see text). In each plot, the data are divided into pre-MCO (light blue), MCO (orange), and post MMCT (dark blue), and the uncertainty on $\delta^{18}O_{sw}$ is ±0.275‰ (at 68% confidence interval) due to the ±1°C uncertainty (at 68% confidence interval) of the Mg/Ca-temperature calibration used by *Lear et al.* [2010]. The black line describes the most likely relationship between the *x* and *y* variables (the probability maximum) given the uncertainty in these variables; the light and dark grey areas are the 95% and 68% confidence intervals. Note that the deepwater temperature used to estimate $\delta^{18}O_{sw}$ were calculated using modern seawater Mg/Ca ratio as in *Lear et al.* [2010] and should therefore only be interpreted in terms of relative change.

latitudinal range). In this interpretation, the absence of large ice sheets in the north acts to reduce the size of the reservoir of ice that is sensitive to subtle variations in atmospheric CO_2.

Next we assess associations between CO_2 variability during the middle Miocene and rapid changes in ice sheet behavior by comparing our record with the ANDRILL records from the Antarctic margin. This task is not straightforward because of the lack of orbitally resolved age models both for the ANDRILL core and at Site 761. These uncertainties mean that we cannot directly correlate the detailed structure seen in our δ^{11}B-CO_2 record with individual cycles in ice sheet behavior reconstructed from the ANDRILL records. Using the best stratigraphic age controls available, however, the two intervals of inferred dramatic ice sheet retreat (at ~15.7 Ma and ~16.4 Ma; colored bands on Figure 4) [*Acton et al.*, 2008–2009; *Feakins et al.*, 2012; *Fielding et al.*, 2011; *Passchier et al.*, 2011; *Warny et al.*, 2009] fall during the intervals of high-amplitude variability in both obliquity and atmospheric CO_2, (Figure 4), suggesting that warm summers brought about by a combination of high tilt and high CO_2 are responsible for the retreat of the Antarctic ice sheet in the middle

Miocene. Further work on both the chronostratigraphy and paleoclimate history of AND-2A is needed to test this hypothesized relationship between atmospheric CO_2 and the stability of the Antarctic ice sheet.

In Figure 5, we compare CO_2 and ice volume between 12 and 17 Myr by constructing crossplots of $\delta^{11}B$ and CO_2 forcing against $\delta^{18}O_{sw}$ (reconstructed from the benthic oxygen isotope record from which the temperature effect has been removed using Mg/Ca paleothermometry [*Lear et al.*, 2010]). We note that at low levels of carbonate saturation, Mg/Ca in benthic foraminiferal calcite also responds to changes in carbonate saturation state [*Elderfield et al.*, 2006; *Yu and Elderfield*, 2007]. Uncertainties surrounding the threshold level of this effect led [*Lear et al.*, 2010] to calculate bottom water temperatures for two assumed scenarios, one in which Mg/Ca is unaffected by changes in saturation state and one in which Mg/Ca is affected by changes in saturation state. For the latter scenario, paired Mg/Ca and Li/Ca records were used to correct for this effect. While that study demonstrated the potential of using paired trace metal records to correct for changes in carbonate saturation state, it is important to acknowledge that uncertainties remain regarding the species-specific sensitivities and thresholds to both temperature and saturation state [*Kender et al.*, 2014; *Lear et al.*, 2010]. Nevertheless, here we plot the $\delta^{18}O_{sw}$ calculated for both scenarios by *Lear et al.* [2010] to compare with our new CO_2 record. The Mg/Ca temperatures are based on modern seawater Mg/Ca, and therefore, the record should only be taken as an indication of $\delta^{18}O_{sw}$ variability. In order to better quantify the relationship between the $\delta^{11}B/CO_2$ forcing and $\delta^{18}O_{sw}$, we follow a probabilistic approach similar to *Foster and Rohling* [2013] to fully account for the uncertainty in *x* and *y* variables. This entailed generating 10,000 realizations of each data set by randomly perturbing each data point within its uncertainty (see Figure 5 caption for more details). Nonparametric regressions (locally weighted scatterplot smoothing (LOWESS)) were fitted to each realization, and the distributions of LOWESS curves at each $\delta^{11}B/CO_2$ forcing step were assessed, and the probability maximum, as well as the 68% and 95% probability intervals, was determined. Importantly, because we are only concerned here with the relative change in climate forcing, it is not necessary to propagate all of the uncertainties in CO_2 discussed above. For instance, while the absolute value of $\delta^{11}B_{sw}$ during the middle Miocene is uncertain ($37.82 \pm 0.7‰$), given the oceanic residence time of boron, it is unlikely to change across our study interval and so can be ignored. Similarly, the uncertainty on the Mg/Ca-based temperature is largely due to the correction in the Mg/Ca of seawater, which is uncertain in the middle Miocene but unlikely to vary significantly across the study interval (the residence time of Mg and Ca is 14 and 1 Ma, respectively), and so our SST uncertainty can be reduced to ±1°C (reflecting the analytical uncertainty in Mg/Ca measurement). Finally, studies of the Quaternary glacial-interglacial cycles suggest that whole ocean alkalinity does not vary on these time scales by more than ±150 μmol/kg [*Hain et al.*, 2010]; given that this is likely an extreme case, we therefore reduce the total alkalinity uncertainty to ±200 μmol/kg to cover the likely change in this variable across our record.

This treatment of the data clearly reveals a curvilinear relationship between $\delta^{11}B/CO_2$ forcing and ice volume, regardless of our choice of corrected or uncorrected $\delta^{18}O_{sw}$ (Figure 5). The inflection point on these nonparametric regressions can be used to identify two distinct $\delta^{18}O_{sw}/CO_2$ forcing regimes (Figure 5). Regime I is characterized by comparatively low levels of atmospheric CO_2 values and a near-linear relationship between increasing CO_2 and decreasing ice volume ($\delta^{18}O_{sw}$) while Regime II is characterized by higher CO_2 but no additional change in ice volume. While ice existed on the continents of the northern hemisphere from at least Eocene/Oligocene boundary time [*Eldrett et al.*, 2007], the global ice budget was almost certainly dominated by the Antarctic ice sheets until the late Pliocene [*Bailey et al.*, 2013; *DeConto et al.*, 2008; *Rohling et al.*, 2014]. Thus, there may have been a small contribution to the global ice budget from the northern hemisphere during the intervals of peak $\delta^{18}O_{sw}$ (greatest ice volumes) during the mid-Miocene Climatic Transition, but during the MCO, it is likely that the ice sheet variability traced by the changes in $\delta^{18}O_{sw}$ captures the waxing and waning of Antarctic ice sheets. The marine-based West Antarctic ice sheet today is certainly the most dynamic component of the Antarctic ice sheet system [*Pollard and DeConto*, 2009]; however, recent ice-proximal provenance studies suggest that during the Pliocene Epoch (3–5 Ma), parts of the East Antarctic ice sheet may also have acted as a dynamic reservoir [*Cook et al.*, 2013; *Mengel and Levermann*, 2014]. Most of the data from the MCO lie in Regime II, or on the upper part of the steep limb that defines Regime I (Figure 5), suggesting that during this time interval, two reservoirs of ice existed, one of which was stable (i.e., no change in $\delta^{18}O_{sw}$ for a given change in CO_2), even at the highest CO_2 levels seen in our record and another that is more dynamic at these low CO_2 levels than predicted by the results of classic coupled climate-Antarctic ice sheet models [*Pollard and DeConto*, 2005].

4. Conclusions

Our new $\delta^{11}B$ record indicates that high-amplitude CO_2 variations accompanied the orbitally paced climatic changes observed in a range of climate records during the middle Miocene. In particular, we show, using the best stratigraphic information available, that the two intervals of Antarctic ice sheet retreat identified in the AND-2A ANDRILL core occur during the MCO when the amplitudes of CO_2 and orbital obliquity variability are both high. A lack of late Pleistocene-like ice sheets in the northern hemisphere indicates that while the overall climatic response to CO_2 change was muted in the middle Miocene, our results also indicate that there was a component of the continental ice budget, most likely on Antarctic, that was responding to CO_2. In detail, our results point to the existence of two reservoirs of ice on Antarctica during the Miocene, one that is stable even at comparatively high CO_2 levels and one that is dynamic at the lower end of the CO_2 range reconstructed. While our data do not distinguish the separated reservoirs, in light of the magnitude of $\delta^{18}O_{sw}$ variability, we hypothesize the existence of a multicomponent Antarctic ice sheet with at least one component (including a portion of the East Antarctic ice sheet), showing significant ice sheet variability at CO_2 concentrations lower than the threshold predicted by coupled climate-ice sheet models [*Cook et al.*, 2013; *Gasson et al.*, 2014; *Mengel and Levermann*, 2014; *Pollard and DeConto*, 2005]. An important implication of this finding is that present-day continental ice masses may become increasingly dynamic as the Earth system approaches equilibrium with anthropogenic climate forcing.

Acknowledgments

This work used samples provided by (I)ODP, which is sponsored by the U.S. National Science Foundation and participating countries under the management of Joint Oceanographic Institutions, Inc. We thank W. Hale and A. Wuelbers of the Bremen Core Repository for their kind assistance. The work was supported by NERC grants NE/I006176/1 (G.L.F. and C.H. L.), NE/I006427/1 (C.H.L), and NE/I006168/1 (P.A.W) and a NERC studentship (R.G). Matthew Cooper, J. Andy Milton, and the B-team are acknowledged for their assistance in the laboratory, and Steve Bohaty, Heiko Pälike, Diederik Liebrand, Wendy Kordesch, and Thomas Chalk are thanked for their helpful suggestions and comments. Reviews from Jimin Yu and two anonymous reviewers also greatly improved this manuscript. The data are available at Paleoceanography as a supplement.

References

Acton, G., et al. (2008–2009), Preliminary Integrated Chronostratigraphy of the AND-2A Core, ANDRILL Southern McMurdo Sound Project, Antarctica, *Terra Antarctica*, *15*(1), 211–220.

Anand, P., H. Elderfield, and M. H. Conte (2003), Calibration of Mg/Ca thermometry in planktonic foraminifera from a sediment trap time series, *Paleoceanography*, *18*(2), 1050, doi:10.1029/2002PA000846,.

Badger, M. P. S., C. H. Lear, R. D. Pancost, G. L. Foster, T. R. Bailey, M. J. Leng, and H. A. Abels (2013), CO_2 drawdown following the middle Miocene expansion of the Antarctic Ice Sheet, *Paleoceanography*, *28*, 42–53, doi:10.1002/palo.20015.

Bailey, I., G. Hole, G. L. Foster, P. A. Wilson, C. Storey, C. Trueman, and M. Raymo (2013), An alternative suggestion for the Pliocene onset of major northern hemisphere glaciation based on the geochemical provenance of North Atlantic Ocean ice-rafted debris, *Quat. Sci. Rev.*, *75*, 181–194.

Billups, K., and D. P. Schrag (2002), Paleotemperatures and ice volume of the past 27 Myr revisited with paired Mg/Ca and $^{18}O/^{16}O$ measurements on benthic foraminifera, *Paleoceanography*, *17*(1), 1003, doi:10.1029/2000PA000567.

Catanzaro, E. J., C. Champion, E. Garner, G. Marinenko, K. Sappenfield, and S. W. Shields (1970), *Boric Acid: Isotopic and Assay Standard Reference Materials NBS (US) Special Publications*, National Bureau of Standards, Institute for Materials Research, Washington, D. C.

Cook, C. P., et al. (2013), Dynamic behaviour of the East Antarctic ice sheet during Pliocene warmth, *Nat. Geosci.*, *6*, 765–769.

DeConto, R. M., D. Pollard, P. A. Wilson, H. Pälike, C. H. Lear, and M. Pagani (2008), Thresholds for Cenozoic bipolar glaciation, *Nature*, *455*, 652–656.

Dickson, A. G. (1990), Thermodynamics of the dissociation of boric acid in synthetic seawater from 273.15 to 318.15 K, *Deep-Sea Res. A. Oceanogr.*, *37*, 755–766.

Elderfield, H., J. Yu, P. Anand, T. Kiefer, and B. Nyland (2006), Calibrations for benthic foraminiferal Mg/Ca paleothermometry and the carbonate ion hypothesis, *Earth Planet. Sci. Lett.*, *250*, 633–649.

Eldrett, J. S., I. C. Harding, P. A. Wilson, E. Butler, and A. P. Roberts (2007), Continental ice in Greenland during the Eocene and Oligocene, *Nature*, *446*, 176–179.

Feakins, S. J., S. Warny, and J.-E. Lee (2012), Hydrologic cycling over Antarctica during the middle Miocene warming, *Nat. Geosci.*, *5*(8), 557–560.

Fielding, C. R., G. H. Browne, B. Field, F. Florindo, D. M. Harwood, L. A. Krissek, R. H. Levy, K. S. Panter, S. Passchier, and S. F. Pekar (2011), Sequence stratigraphy of the ANDRILL AND-2A drillcore, Antarctica: A long-term, ice-proximal record of Early to Mid-Miocene climate, sea-level and glacial dynamism, *Palaeogeogr. Palaeoclimatol. Palaeoecol.*, *305*(1–4), 337–351.

Foster, G. L. (2008), Seawater pH, pCO_2 and $[CO_3^{2-}]$ variations in the Caribbean Sea over the last 130 kyr: A boron isotope and B/Ca study of planktic forminifera, *Earth Planet. Sci. Lett.*, *271*(1–4), 254–266.

Foster, G. L., and E. J. Rohling (2013), Relationship between sea level and climate forcing by CO_2 on geological timescales, *Proc. Natl. Acad. Sci. U.S.A.*, *110*(4), 1209–1214.

Foster, G. L., P. A. E. Pogge von Strandmann, and J. W. B. Rae (2010), Boron and magnesium isotopic composition of seawater, *Geochem. Geophys. Geosyst.*, *11*, Q08015, doi:10.1029/02010GC003201.

Foster, G., C. H. Lear, and J. Rae (2012), The evolution of pCO_2, ice volume and climate during the middle Miocene, *Earth Planet. Sci. Lett.*, *341–344*, 243–254.

Gasson, E., et al. (2014), Uncertainties in the modelled CO_2 threshold for Antarctic glaciation, *Clim. Past*, *10*, 451–466.

Hain, M. P., D. M. Sigman, and G. H. Haug (2010), Carbon dioxide effects of Antarctic stratification, North Atlantic Intermediate Water formation, and subantarctic nutrient drawdown during the last ice age: Diagnosis and synthesis in a geochemical box model, *Global Biogeochem. Cycles*, *24*, GB4023, doi:10.1029/2010GB003790.

Hays, J., J. Imbrie, and N. Shackleton (1976), Variations in Earth's orbit - Pacemaker of Ice Ages, *Science*, *194*(4270), 1121–1132.

Henehan, M. J., et al. (2013), Calibration of the boron isotope proxy in the planktonic foraminifera Globigerinoides *ruber* for use in palaeo-CO_2 reconstruction, *Earth Planet. Sci. Lett.*, *364*(0), 111–122.

Holbourn, A., W. Kuhnt, J. Simo, and Q. Li (2004), Middle Miocene isotope stratigraphy and paleoceanographic evolution of the northwest and southwest Australian margins (Wombat Plateau and Great Australian Bight), *Palaeogeogr. Palaeoclimatol. Palaeoecol.*, *208*, 1–22.

Holbourn, A., W. Kuhnt, M. Schulz, J. Flores, and N. Andersen (2007), Orbitally-paced climate evolution during the middle Miocene "Monterey" carbon-isotope excursion, *Earth Planet. Sci. Lett.*, *261*, 534–550.

Holbourn, A., W. Kuhnt, M. Lyle, L. Schneider, O. Romero, and N. Andersen (2014), Middle Miocene climate cooling linked to intensification of eastern equatorial Pacific upwelling, *Geology*, doi:10.1130/G34890.34891.

Horita, J., H. Zimmermann, and H. D. Holland (2002), Chemical evolution of seawater during the Phanerozoic: Implications from the record of marine evaporites, *Geochim. Cosmochim. Acta*, *66*(21), 3733–3756.

Imbrie, J., et al. (1993), On the structure and origin of major glaciation cycles 2. The 100,000-year cycle, *8*(6), 699–735, doi:10.1029/93PA02751.

Kender S., J. Yu, and V. L. Peck (2014), Deep ocean carbonate ion increase during mid Miocene CO_2 decline, *Sci. Rep.*, *4*, 4187, doi:10.1038/srep04187.

Köhler, P., R. Bintanja, H. Fischer, F. Joos, R. Knutti, G. Lohmann, and V. Masson-Delmotte (2010), What caused Earth's temperature variations during the last 800,000 years? Data-based evidence on radiative forcing and constraints on climate sensitivity, *Quat. Sci. Rev.*, *29*(1–2), 129–145.

Kürschner, W. M., Z. Kvaček, and D. L. Dilcher (2008), The impact of Miocene atmospheric carbon dioxide fluctuations on climate and the evolution of terrestrial ecosystems, *Proc. Natl. Acad. Sci. U.S.A.*, *105*(2), 449–453.

Laskar, J., P. Robutel, F. Joutel, M. Gastineau, A. C. M. Correia, and B. Levrard (2004), A long-term numerical solution for the insolation quantities of the Earth, *Astron. Astrophys.*, *428*(1), 261–285.

Lear, C. H., E. M. Mawbey, and Y. Rosenthal (2010), Cenozoic benthic foraminiferal Mg/Ca and Li/Ca records: Toward unlocking temperatures and saturation states, *Paleoceanography*, *25*, PA4215, doi:10.1029/2009PA001880.

Lemarchand, D., J. Gaillardet, E. Lewin, and C. J. Allegre (2002), Boron isotope systematics in large rivers: Implications for the marine boron budget and paleo-pH reconstruction over the Cenozoic, *Chem. Geol.*, *190*(1–4), 123–140.

Lisiecki, L., and M. Raymo (2005), A Pliocene-Pleistocene stack of 57 globally distributed benthic $\delta^{18}O$ records, *Paleoceanography*, *20*, PA1003, doi:10.1029/2004PA001071.

Lüthi, D., et al. (2008), High-resolution carbon dioxide concentration record 650,000-800,000 years before present, *Nature*, *453*(7193), 379–382.

Mengel, M., and A. Levermann (2014), Ice plug prevents irreversible discharge from East Antarctica, *Nat. Clim. Change*, *4*, 451–455.

Myhre, G., E. J. Highwood, K. P. Shine, and F. Stordal (1998), New estimates of radiative forcing due to well mixed greenhouse gases, *Geophys. Res. Lett.*, *25*(14), 2715–2718, doi:10.1029/98GL01908.

Passchier, S., G. Browne, B. Field, C. R. Fielding, L. A. Krissek, K. Panter, S. F. Pekar, and ANDRILL-SMS Science Team (2011), Early and middle Miocene Antarctic glacial history from the sedimentary facies distribution in the AND-2A drill hole, Ross Sea, Antarctica, *Geol. Soc. Am. Bull.*, *123*(11–12), 2352–2365.

Passchier, S., C. J. Falk, and F. Florindo (2013), Orbitally-paced shifts in the particle size Antarctic continental shelf sediments in response to ice dynamics during the Miocene Climatic Optimum, *Geosphere*, *9*(1), 54–62.

Pollard, D., and R. M. DeConto (2005), Hysteresis in Cenozoic Antarctic ice-sheet variations, *Global Planet. Change*, *45*, 9–21.

Pollard, D., and R. M. DeConto (2009), Modelling West Antarctic ice sheet growth and collapse through the past five million years, *Nature*, *458*, 329–332.

Rohling, E. J., G. L. Foster, K. M. Grant, G. Marino, A. P. Roberts, M. E. Tamisiea, and F. Williams (2014), Sea-level and deep-sea-temperature variability over the past 5.3 million years, *Nature*, *508*, 477–482.

Sanyal, A., M. Nugent, R. J. Reeder, and J. Buma (2000), Seawater pH control on the boron isotopic composition of calcite: Evidence from inorganic calcite precipitation experiments, *Geochim. Cosmochim. Acta*, *64*(9), 1551–1555.

Sanyal, A., J. Bijma, H. Spero, and D. W. Lea (2001), Empirical relationship between pH and the boron isotopic composition of Globigerinoides sacculifer: Implications for the boron isotope paleo-pH proxy, *Paleoceanography*, *16*(5), 515–519, doi:10.1029/2000PA000547.

Schlitzer, R. (2000), Electronic atlas of WOCE hydrographic and tracer data now available, *Eos Trans. AGU*, *81*(5), 45–45, doi:10.1029/00EO00028.

Shackleton, N. (2000), The 100,000-year ice-age cycle identified and found to lag temperature, carbon dioxide, and orbital eccentricity, *Science*, *289*(5486), 1897–1902.

Shevenell, A. E., J. P. Kennett, and D. W. Lea (2004), Middle Miocene Southern Ocean cooling and Antarctic cryosphere expansion, *Science*, *305*(5691), 1766–1770.

Sime, N. G., C. L. De La Rocha, E. T. Tipper, A. Tripati, A. Galy, and M. J. Bickle (2007), Interpreting the Ca isotope record of marine biogenic carbonates, *Geochim. Cosmochim. Acta*, *71*(16), 3979–3989.

Takahashi, T., et al. (2009), Climatological mean and decadal change in surface ocean pCO_2, and net sea-air CO_2 flux over the global oceans, *Deep Sea Res., Part I*, *56*(11), 2075–2076.

Warny, S., R. A. Askin, M. J. Hannah, B. A. R. Mohr, J. I. Raine, D. M. Harwood, F. Florindo, and the SMS Science Team (2009), Palynomorphs from a sediment core reveal a sudden remarkably warm Antarctica during the middle Miocene, *Geology*, *37*(10), 955–958.

You, Y., M. Huber, R. D. Muller, C. J. Poulsen, and J. Ribbe (2009), Simulation of the Middle Miocene Climate Optimum, *Geophys. Res. Lett.*, *36*, L04702, doi:10.1029/2008GL036571.

Yu, J., and H. Elderfield (2007), Benthic foraminiferal B/Ca ratios reflect deep water carbonate saturation state, *Earth Planet. Sci. Lett.*, *258*, 73–86.

Zachos, J. C., G. R. Dickens, and R. E. Zeebe (2008), An early Cenozoic perspective on greenhouse warming and carbon-cycle dynamics, *Nature*, *451*(7176), 279–283.

Zhang, Y. G., M. Pagani, Z. H. Liu, S. Bohaty, and R. DeConto (2013), A 40-million-year history of atmospheric CO_2, *Phil. Trans. R. Soc. A.*, *371*, doi:10.1098/rsta.2013.0096.